Modelling the long-term hydro-mechanical behaviour of a bentonite pellet/powder mixture with consideration of initial structural heterogeneities

Nadia Mokni, Agustín Molinero Guerra, Yu-Jun Cui, Pierre Delage, Patrick Aimedieu, Michel Bornert, Anh Minh A.M. Tang

Modelling the long-term hydro-mechanical behaviour of a bentonite pellet/powder mixture with consideration of initial structural heterogeneities

NADIA MOKNI*, AGUSTÍN MOLINERO GUERRA†‡, YU-JUN CUI†, PIERRE DELAGE†, PATRICK AIMEDIEU†, MICHEL BORNERT† and ANH MINH TANG†

The aim of this paper is to investigate the long-term hydro-mechanical behaviour of a highly heterogeneous MX80 bentonite pellet/powder mixture (80/20 in dry mass), which is one of the candidate sealing materials in deep geological repositories. In spite of the operational advantages related to the use of the mixture, structural heterogeneities resulting from the installation process constitute a matter of concern and require special approaches to describe adequately the material behaviour during hydration. In this study, a double structure formulation taking into account the initial structural heterogeneity of the material as well as damage to pellets upon wetting is proposed. The formulation is applied to the modelling of a 1/10 mock-up of Sealex large-scale tests. Hydraulic and mechanical parameters are determined from an extensive laboratory programme carried out on a single pellet of bentonite and on the pellet/powder mixture. To ensure an adequate analysis of the test, the initial heterogeneous structural distribution of the material is determined by image analysis of microfocus X-ray computed tomography observations. The model allows the anisotropic swelling behaviour of the mixture to be satisfactorily reproduced when accounting for the spatial variation of the material's initial porosity. In particular, the long-term (decade) hydro-mechanical behaviour of the mixture can be well described. Detailed analysis of the modelling results demonstrates the existence of dry density gradients at the long term and their influence on swelling pressure anisotropy.

KEYWORDS: expansive soils; fabric/structure of soils; numerical modelling; radioactive waste disposal

INTRODUCTION

Most European concepts for deep geological disposal of high- and intermediate-level, long-lived radioactive waste involve bentonite-based materials as buffers, backfills and seals of disposal galleries and access shafts/ramps to ensure isolation and containment of the waste from the biosphere. The swelling pressures of buffers, backfills and seals are requirements for these components to achieve safety. One of the major roles of swelling is to ensure that the buffer is self-sealing and closes technological gaps and macro-voids. It is well documented that the swelling pressure depends principally on the dry density of the material (Imbert & Villar, 2006). Accordingly, a relatively small change in density can induce significant changes in swelling pressure. That is why most laboratory and large-scale tests have focused on achieving the required average dry density. However, very few experiments have focused on the dry density heterogeneities at initial state and in the course of hydration, and their influence on swelling pressure. It is worth noting that this dry density homogenisation can last for a long time. For instance, while dismantling the engineered barrier (EB) emplacement experiment where two types of bentonite with different dry densities had been emplaced (blocks and pellets of bentonite), some heterogeneity in terms of dry density and water content distributions was observed after almost 10 years of hydration (Wieczorek et al., 2017).

In order to investigate the long-term homogenisation of bentonite-based seals, the French Institute of Radiation protection and nuclear safety (IRSN) has launched the Sealex project, which relies on a series of in situ experiments in IRSN's underground research laboratory (URL, Tournemire, France) (Mokni, 2016; Mokni & Barnichon, 2016; Mokni & Barnichon, 2016). Based on the design of the in situ experiments, laboratory mock-up tests (one-tenth scale) were also performed with the aim of investigating the distribution of dry density due to water saturation.

Sealex in situ and mock-up tests were conducted on MX80 bentonite pellet/powder mixture which is one of the candidate sealing materials because of its low permeability, high radionuclide retardation capacity and its high swelling potential upon hydration (Pusch, 1979; Yong et al., 1986; Villar, 2008). This material, corresponding to a mixture of bentonite powder and highly compacted bentonite pellets, is initially obviously highly heterogeneous. The degree and distribution of heterogeneities will vary during hydration and the average dry density might not be sufficient to characterise its final state and containment performance. Low-density zones can remain within the buffer mixture, potentially enhancing the transport of radionuclides in the long repository exploration period.

For the long-term safety assessment of the repository, it is essential to predict the evolution and the final state of the initially heterogeneous seal and to evaluate the effects of remaining density gradients and swelling pressure differences within the emplaced mixture on the seal hydro-mechanical behaviour. To this end, an appropriate constitutive

* Institut de Radioprotection et Sûreté Nucléaire (IRSN), Fontenay-aux-Roses, France (Orcid:0000-0003-1944-9118).
† Ecole des Ponts ParisTech, Laboratoire Navier/CERMES, Marne La Vallée, France.
‡ Institut de Radioprotection et de Sûreté Nucléaire (IRSN), Fontenay-aux-Roses, France.

hydro-mechanical model that accounts for spatial and temporal distributions of the relevant properties of the bentonite pellet/powder is fundamental.

Another important characteristic of the bentonite pellet/powder mixture is the multimodal nature of its porous network, which governs all of its hydro-mechanical properties. This aspect has been considered in several hydro-mechanical constitutive models (e.g. Gens & Alonso, 1992; Alonso et al., 1999, 2011; Sanchez et al., 2005; Gens et al., 2011). However, the initial heterogeneities have often been neglected.

In this study, a hydro-mechanical model which takes into account the initial heterogeneous distribution and multi-modal nature of the bentonite pellet/powder mixture is developed. Moreover, the model accounts for transient microstructural features characterising the high-density bentonite pellets. A description of microstructural characteristics of the pellet/powder mixture is first given, providing a background for the model development. The proposed model is then outlined and used to model the mock-up test. The model parameters were determined essentially based on the back-analysis of laboratory test results. Special attention has been devoted to the swelling anisotropy features identified experimentally.

INSIGHTS INTO MICRO- AND MACROSTRUCTURAL FEATURES
Tested material
The investigated material is a mixture of pellets and powder of MX80 bentonite (Wyoming, USA) with a proportion of 80 pellets/20 powder in dry mass prepared at a dry density, $\rho_d = 1.49 \, \text{Mg/m}^3$. The material has a high smectite content (80%) with some inclusions of non-clayey minerals (quartz – 4% of the total mass; muscovite – 4% of the total mass; pyrite – less than 1% of the total mass; and some elements of calcite). The cation exchange capacity (CEC) is 98 meq/100 g, with Na^+ as the major exchangeable cation. The liquid limit is 560%, the plastic limit is 62% and the unit mass is $2.77 \, \text{Mg/m}^3$ (Saba et al., 2014a). The powder grains present a diameter between 0.8 mm and 2 mm. The initial suction of bentonite powder, $s = 190.9 \, \text{MPa}$, was measured with a chilled mirror dew-point tensiometer (Decagon WP4).

Pellets were produced by compacting bentonite powder instantaneously into a mould of 7 mm dia. and 7 mm high at a water content of $6 \pm 1\%$ (resulting in a dry density $\rho_d = 2.12 \, \text{Mg/m}^3$, corresponding to a void ratio $e = 0.30 \pm 0.07$). Fig. 1 shows a pellet of bentonite at its initial

state. It has a quasi-cylindrical shape with two spherical poles on top and bottom. Initial suctions of the pellet ($s = 135.5 \pm 3 \, \text{MPa}$) and of the mixture ($s = 138 \, \text{MPa}$) were measured in the laboratory also with a chilled mirror dew-point tensiometer (Decagon WP4).

Microstructural characterisation
The microstructure of a pellet of bentonite at initial state was investigated by means of mercury intrusion porosimetry (MIP) tests (Fig. 2) combined with microfocus X-ray computed tomography (μ-CT) observations (Fig. 3). At initial state, a monomodal distribution is observed corresponding to the micro-pores with a dominant peak at 11.9 nm (Fig. 2) and representing 93.2% of total porosity. Another pore population at diameters around 4–5 μm representing 6.8% of the total porosity is also identified. This population corresponds to cracks within the pellet (Molinero-Guerra et al., 2017). The network of cracks is also visible in Fig. 3(a).
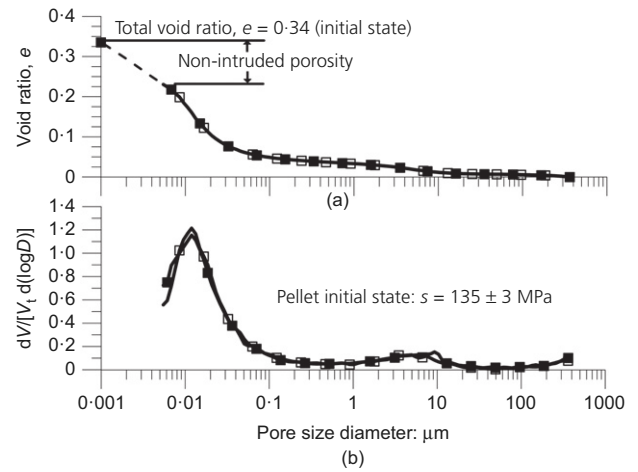

Fig. 2. MIP test results for a pellet of bentonite at its initial state

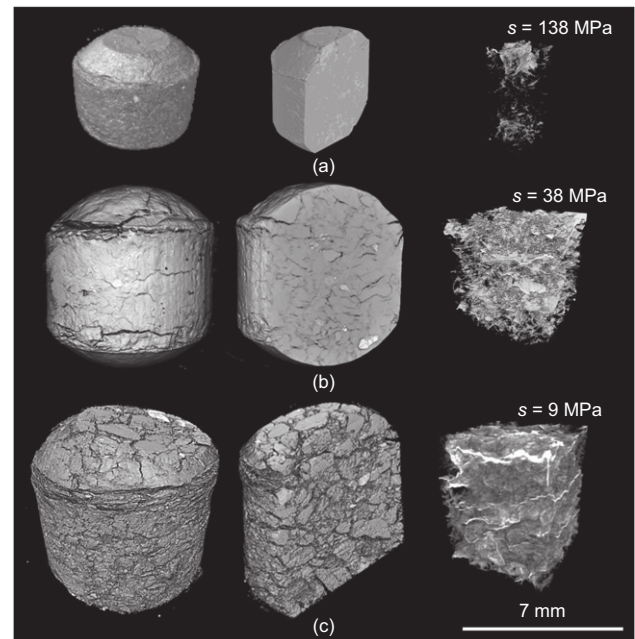Fig. 1. Pellet at its initial state

Fig. 3. X-ray computed microtomography (μ-CT) observations (4.41 μm/voxel) – 3D reconstruction image and network of cracks: (a) $s = 138 \, \text{MPa}$; (b) $s = 38 \, \text{MPa}$; (c) $s = 9 \, \text{MPa}$

Several pore size distribution (PSD) curves (Figs 4–6) of pellets equilibrated at different suctions were determined, together with the μ-CT observations (Fig. 3). The changes in suction of the pellets were made by placing them in desiccators containing saturated saline solution. The sample was periodically taken out of the desiccator for measuring suction and weight (Molinero-Guerra *et al.*, 2017, 2018c). The PSD curves were obtained on freeze-dried samples using an Autopore IV 9500 mercury intrusion porosimeter (Micromeritics) that operates at a maximum pressure of 230 MPa, corresponding to a minimum entrance diameter of 0·00542 μm. For μ-CT observations, the X-ray source parameters were 80 kV and 40 μA. Voxel size was 4·41 μm. The samples were scanned using 1440 projections equally spread on 360°. After the reconstruction, 1298 horizontal slices were calculated (16 bit images; 1644 × 1292 pixels).

Interestingly, as suction decreases, two structural levels become distinguishable (Figs 4–6): the micro-pores correspond to intra-aggregate pores and have a size smaller than 3 μm; the macro-pores correspond to inter-aggregate pores and swelling-induced cracks and have a size greater than 3 μm. Here, the depression between the dominant peaks reported in the PSD functions at $s = 1$ MPa (Fig. 5) has been

Fig. 5. MIP test results on a single pellet of bentonite equilibrated under suctions from 25 to 1 MPa: (a) cumulative porosity curves; (b) derivative curve for $s = 25$ MPa; (c) derivative curve for $s = 9$ MPa; (d) derivative curve for $s = 4·2$ MPa; (e) derivative curve for $s = 1$ MPa
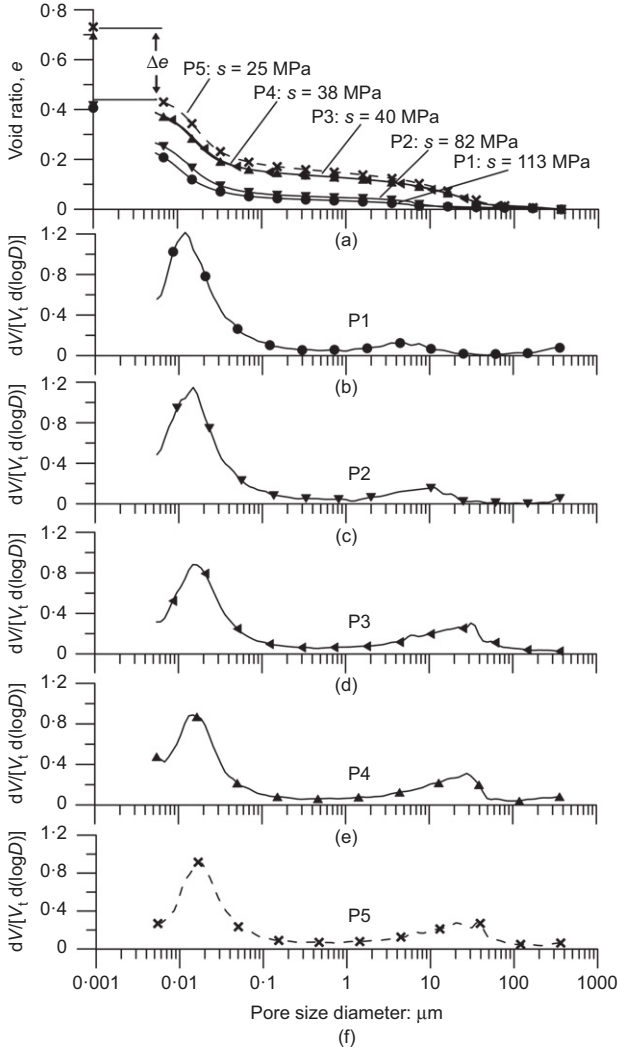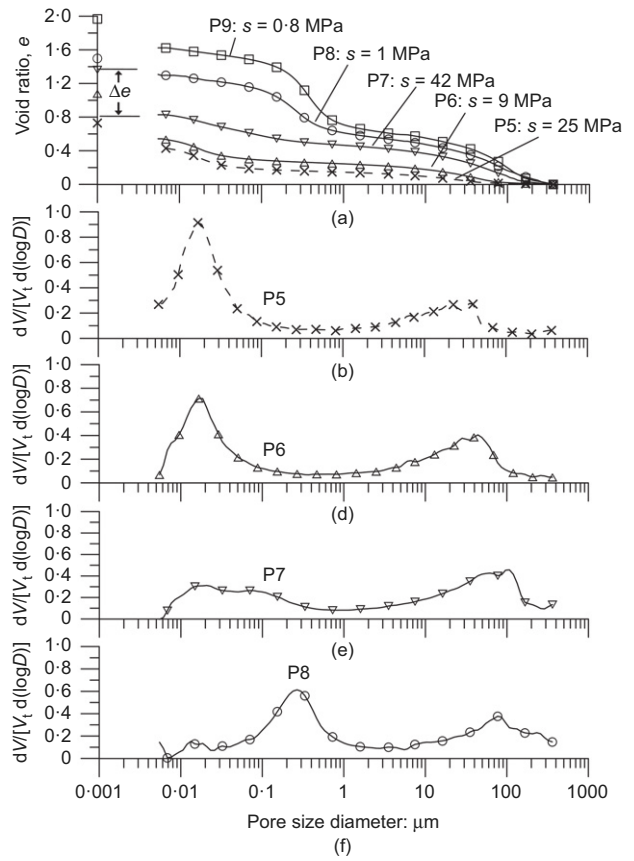
Fig. 4. MIP test results on a single pellet of bentonite equilibrated under suctions from 113 to 25 MPa: (a) cumulative porosity curves; (b) derivative curve for $s = 113$ MPa; (c) derivative curve for $s = 82$ MPa; (d) derivative curve for $s = 40$ MPa; (e) derivative curve for $s = 38$ MPa; (f) derivative curve for $s = 25$ MPa
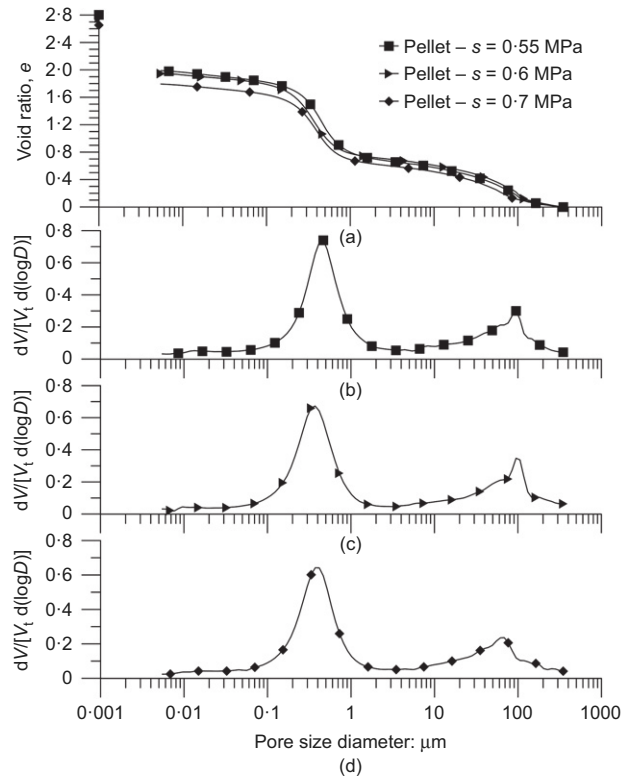
Fig. 6. MIP test results on a single pellet of bentonite equilibrated under suctions from 0·55 to 0·7 MPa: (a) cumulative porosity curves; (b) derivative curve for $s = 0·55$ MPa; (c) derivative curve for $s = 0·6$ MPa; (d) derivative curve for $s = 0·7$ MPa

used as the limiting entrance pore size separating micro- and macro-porosity (3 µm).

Figure 4(a) shows that no significant swelling is observed between the initial state and states at suction larger than 82 MPa, whereas swelling due to the developments of pores in the range 10–40 µm is observed between 82 and 25 MPa. For lower suctions, the curve at 4·2 MPa (Fig. 5(d)) looks like a transition with a decrease in the peak previously observed at 19 nm (Figs 5(b) and 5(c)) and the development of pores with a diameter up to 400 nm. At very low suction (Fig. 6), no significant porosity is observed below 100 nm. The significant swelling is due to the development of pores with average diameters of 290 nm (suction 1 MPa) and 400 µm (suction 0·7 MPa). No significant changes are observed between $s = 0·7$ and 0·55 MPa.

Three-dimensional (3D) reconstructions of pellets at initial state, and hydrated at 38 and 9 MPa, are shown in Fig. 3, providing a view of the global changes of the pellets. The hydration at 38 MPa (Fig. 3(b)) evidences the development of some disconnected cracks around and inside the pellet, particularly at the top. At 9 MPa suction (Fig. 3(c)) swelling is due in significant part to the development of an interconnected crack network and bentonite pieces composed within the crack network have comparable density. These observations suggest that the degradation and damage of pellets is dependent on suction. This is consistent with the observation of Wang *et al.* (2013) on highly compacted bentonite-based materials. The swelling of the pellet is hence due to the combined action of crack propagation (better observed by using X-ray µCT) and the expansion of bentonite grains (quantified by MIP).

The MIP tests were performed on the mixture prepared at a dry density $\rho_d = 1·49$ Mg/m³ and saturated under constant-volume conditions. The PSD curves are shown in Fig. 7. Two structural levels can be distinguished: the micro-pores with an average size diameter of 14·9 nm, which is in the range of the small pores detected within a single pellet of bentonite; and macro-pores with an average size diameter of 49·3 µm corresponding to inter-aggregate pores and swelling-induced cracks with sizes greater than 3 µm.

The X-ray µCT observations were performed on the bentonite pellet/powder mixture prepared at $\rho_d = 1·49$ Mg/m³

and $s = 138$ MPa using a special cell in polymethyl methacrylate (PMMA). More details on the experimental testing can be found in Molinero-Guerra *et al.* (2018b). The PMMA cell has 60 mm inner diameter and is 120 mm high (1/10 Sealex in situ tests, see Fig. 8). The objective here is to investigate the initial microstructural distribution of the mixture and its evolution during hydration. Three samples (samples 1, 2 and 3) were prepared by filling the cell by packets corresponding to one layer of pellets spread over the base of the 60 mm dia. cylinder and by adding the corresponding amount of powder (80% pellets and 20% powder). This protocol allowed a relatively homogeneous mixture at the target dry density (Molinero-Guerra *et al.*, 2016a, 2016b).

The vertical sections of the tested samples are shown in Fig. 9(a). Several zones with large, air-filled inter-pellet voids without grains of powder are observed inside and at the top of the sample in the three cases. Fig. 9(b) shows a zoom of an assembly of pellets located 60 mm from the bottom hydration front in the case of sample 1. After 11 days several cracks can be observed within the pellets constituting preferential paths for water infiltration. After 27 days, the pattern of cracks develops, inducing degradation of pellets, and the swollen pellets invade progressively the large interpellet macro-pores. After 56 days of hydration, the granular structure of the mixture disappears, even though some contours can still be identified. More details on the µ-CT observations of the mixture can be found in Molinero-Guerra *et al.* (2018b).

HYDRO-MECHANICAL BEHAVIOUR OF THE MIXTURE IN 1/10 MOCK-UP TEST

A 1/10 mock-up test was performed in order to investigate the long-term behaviour of the bentonite pellet/powder mixture upon hydration (Molinero-Guerra *et al.*, 2018a). The layout of the small-scale infiltration stainless steel cell is presented in Fig. 10. The constant-volume conditions are ensured by a rigid structure. The material is saturated from both the top and the bottom. More details on the experimental set-up can be found in Molinero-Guerra *et al.* (2018a).

Six total pressure sensors measure the radial swelling pressure at different positions in the cell: $h = 20, 40, 60, 80$ and 100 mm, namely, SP20, SP40, SP60, SP80 and SP100, respectively. This configuration allows the evolution of the swelling pressure at different positions to be investigated,

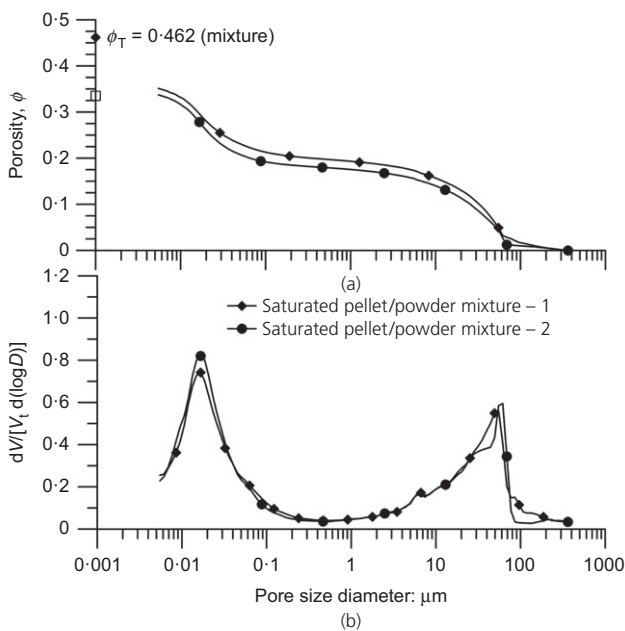**Fig. 7. MIP test results for two specimens of saturated pellet/powder mixture: (a) cumulative porosity curves; (b) derivative curves**
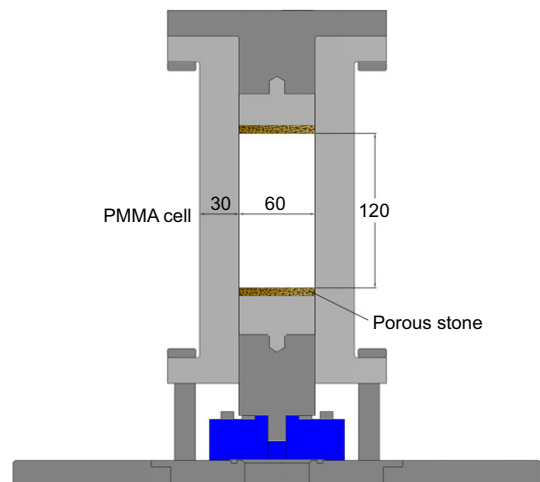
Fig. 8. Layout of the PMMA cell. Cell dimensions are in mm

(a)

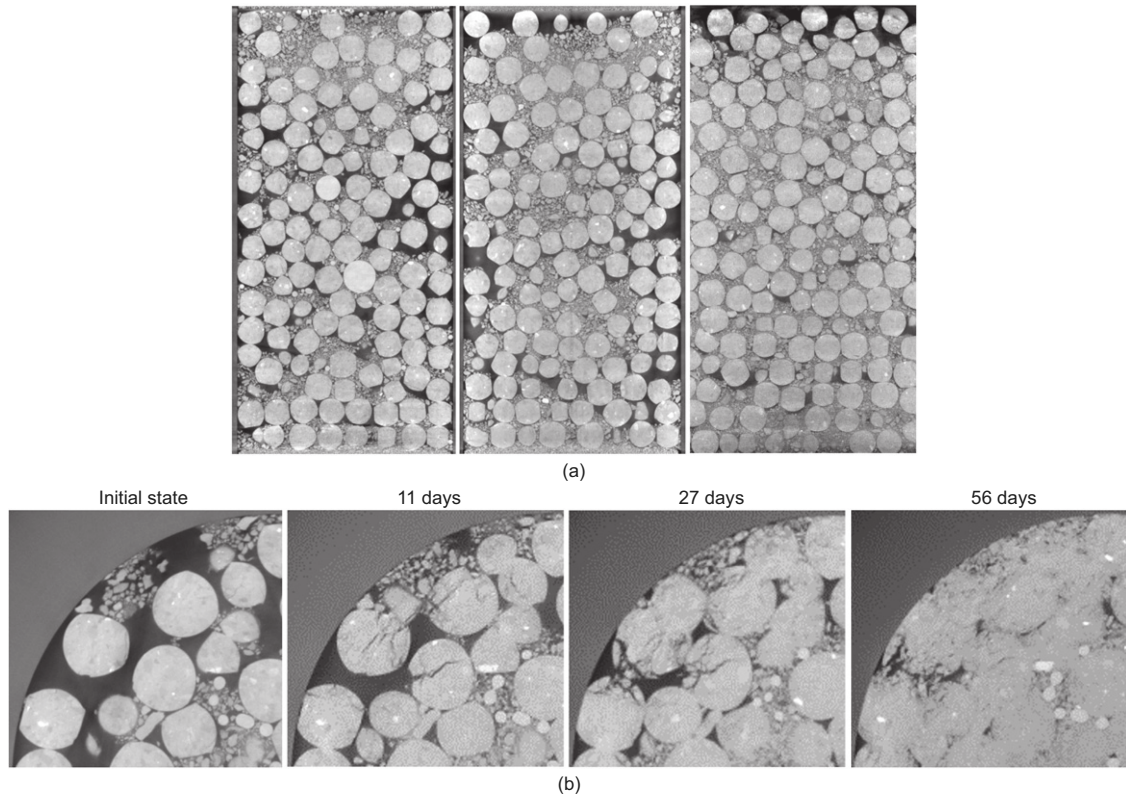| Initial state | 11 days | 27 days | 56 days |

(b)

Fig. 9. (a) μ-CT observations (vertical slices) of three different pellet/powder bentonite mixtures (image resolution is 50 µm/voxel). (b) Zoom at 60 mm from the bottom of sample 1 at different times
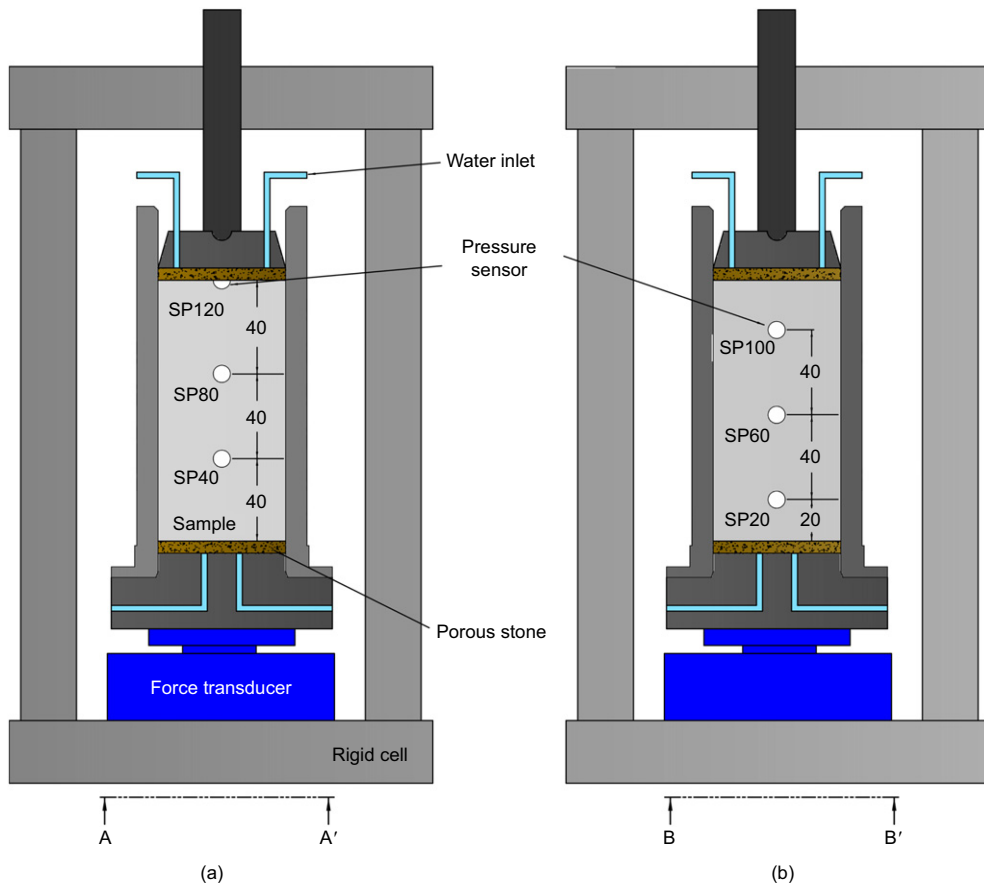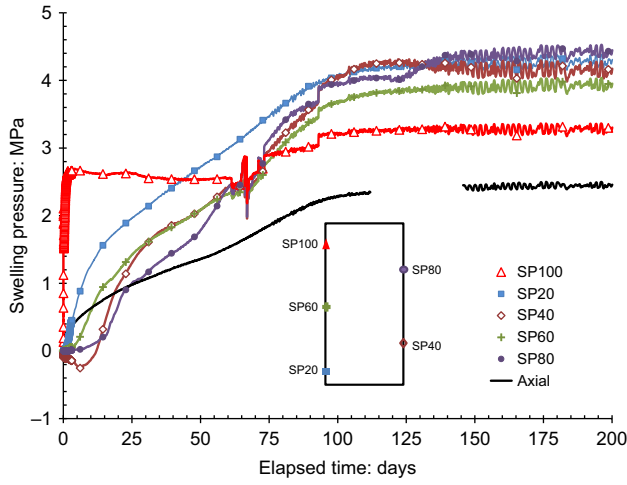

Fig. 10. Layout of the small-scale mock-up test

Fig. 11. Evolution of swelling pressure with time for the pellet/powder bentonite mixture after 200 days of hydration

Fig. 12. Double-structure deformation model for expansive clays: (a) microstructural model; (b) interaction functions

which is crucial for monitoring the evolution of the dry density. A force transducer was installed under the cell base to monitor the axial swelling pressure. Owing to the use of stainless steel cell, no μ-CT scans were possible for the initial state characterisation.

Figure 11 shows the evolution of swelling pressure at different positions after 200 days of hydration. A heterogeneous evolution of swelling pressure is observed, which is due to the distance to the hydration front and the initial heterogeneous pellet/powder distribution. The difference observed between the radial and axial swelling pressure after 200 days of hydration could be attributed to the presence of larger inter-pellet voids at the top of the sample.

A DOUBLE-STRUCTURE HYDRO-MECHANICAL MODEL ACCOUNTING FOR INITIAL HETEROGENEITY AND SWELLING DAMAGE

Mechanical constitutive equations

The basic idea of the model proposed in this paper is the appropriate representation of the initial structural heterogeneities of the mixture together with the wetting-induced damage to the pellets.

The model is based on the distinction within the mixture of pellets and powder of two dominant pore levels (macro- and micro-pores). A large proportion of the micro-pores lies initially in the high-density pellets as observed in Figs 2 and 7 (micro-pores represent 93·2% of the pellets' total porosity (Fig. 2) and for the mixture (Fig. 7) the micro-pores have an average size diameter in the range of the small pores detected within a single pellet of bentonite). The macrostructure refers to the large-scale arrangement of pellets and powder and the large pores between them. This distinction allows the phenomena that affect each pore level and the interaction between them to be accounted for (e.g. Gens & Alonso, 1992; Alonso *et al.*, 2011; Gens *et al.*, 2011).

The macro-pores are considered to be partially filled with liquid phase. The macroscopic transport of liquid takes place in the macro-pores, which are called flowing pores. The total porosity is defined as the sum of macro-porosity ϕ_M and micro-porosity ϕ_m.

In order to account for initial structural heterogeneities, macro-porosity is appropriately represented in each finite element assuming that the micro-porosity is homogeneously distributed. The resulting field has the same mean porosity as the tested mixture. This allows the initial heterogeneous structural distribution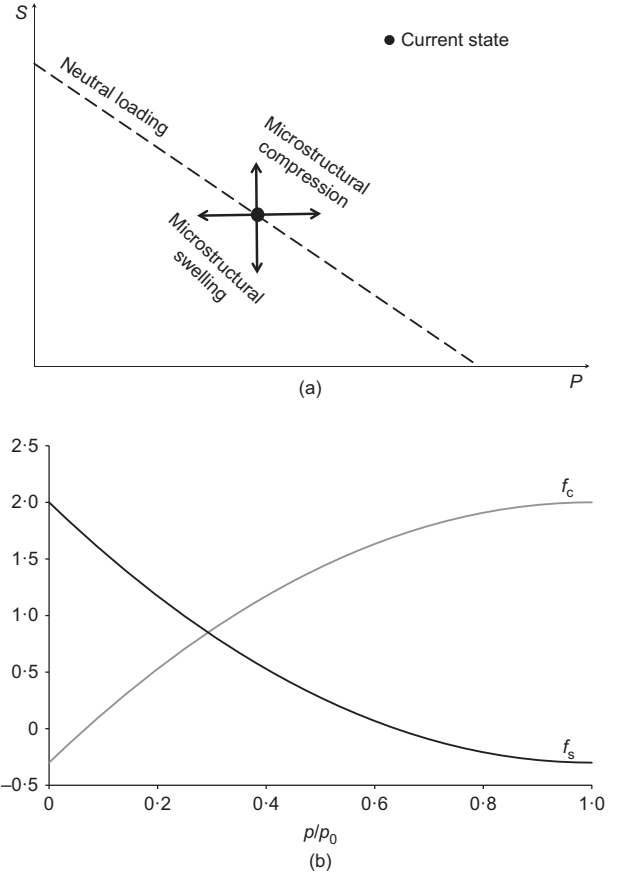 to be accounted for. The spatial variations of total porosity and of dry density within the material are thus represented.

For each finite element a macroscopic volumetric deformation is computed from the mean macro void ratio, e_M^{mean} (Alonso *et al.*, 2006):

$$e_M^{mean} = \frac{\phi_M}{1 - \phi_M} \tag{1}$$

$$\varepsilon_v^M = -\frac{e_M - e_M^{mean}}{1 + e_M^{mean}} \tag{2}$$

where e_M is the macrostructural void ratio of the mixture.

To represent the mechanical behaviour of the material, a double-structure elasto-plastic model for expansive clays is adopted (e.g. Gens & Alonso, 1992; Sanchez *et al.*, 2005; Gens *et al.*, 2011). The model considers deformations at macro- and microstructural levels, and the coupling between them. The model assumes that for the macrostructural level, both elastic and plastic strains can develop as a result of stress and suction changes. The behaviour of the macrostructural level is defined by the Barcelona basic model (BBM) (Alonso *et al.*, 1990).

Considering a heterogeneous distribution of macro-porosity (i.e spatial variation of macro-porosity), the hardening parameter is defined for each finite element as follows

$$P_0^* = P_{0_{mean}}^* \exp\left[\frac{1 + e_M^{mean}}{\lambda(s) - k} \varepsilon_v^M\right] \tag{3}$$

$$\lambda(s) = \lambda(0)\left[r + (1 - r)e^{-\beta s}\right] \tag{4}$$

where $\lambda(s)$ is the slope of the virgin consolidation line at suction s; $\lambda(0)$ is the slope of the virgin saturated
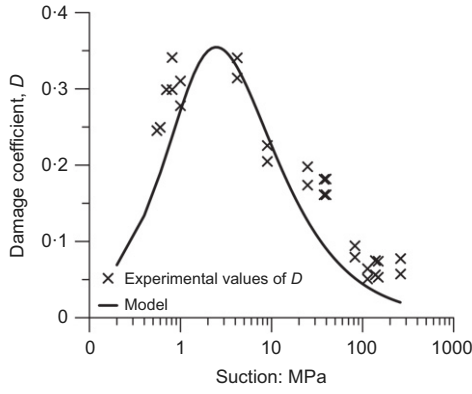
Fig. 13. Damage coefficient, D – experimental results and model fitting

consolidation line; P_0^* is the saturated preconsolidation pressure; k is an elastic parameter for the macrostructure; and r and β model parameters.

A fundamental assumption of the framework is that microstructural behaviour is independent of the macrostructural state and only responds to changes in suction and stress at the microstructural level. The mechanical behaviour at the microstructural level is controlled by mean effective stress defined as (e.g. Gens & Alonso, 1992; Alonso *et al.*, 2011; Gens *et al.*, 2011)

$$\hat{p} = (p + s) \qquad (5)$$

where p is the net stress and s is suction.

The line corresponding to the constant microstructural mean stress in plane (p–s) is referred to as the neutral line (NL), since no microstructural deformation occurs when the stress path moves on it (Fig. 12(a)). The NL line divides the plane into two parts, defining two main generalised stress paths identified as: microstructural swelling (MS) when there is a decrease in $\hat{p}$ and microstructural compression (MC) when there is an increase in $\hat{p}$.

In order to account for crack generation while wetting (Figs 3 and 9(b)), a damage coefficient D is defined as the ratio of generated porosity corresponding to cracks (ϕ_{cracks}) within a single pellet (pores with an average diameter higher than 3 µm) to the total porosity of the pellet at a given suction. The evolution of D as a function of suction is shown in Fig. 13. Here ϕ_{cracks} has been calculated using MIP results (Figs 4–6) for each single pellet equilibrated from the

initial state to a desired suction and considering pores with an average diameter higher than 3 µm. The fitting curve obtained using equation (6) is also shown in the figure.

$$(s) = \frac{\beta_{\text{d}} \ln(\alpha_{\text{d}} s^2 + 1)}{(s + p_{\text{atm}})^{\beta_{\text{d}}/\alpha_{\text{d}}}} \qquad (6)$$

where α_{d}, β_{d} are parameters of the model; s is suction; and p_{atm} is the atmospheric pressure.

The results show that D is dependent on the imposed suction. It increases with decreasing suction, reaching a maximum value at $s = 4{\cdot}2$ MPa. At this stage the pellet has degraded and lost its initial geometry (Fig. 9(b)) and no more cracks develop for lower suctions when reaching saturation.

The microstructural elastic volumetric strain incorporating pellets damage is expressed as

$$d\varepsilon_{\text{vm}}^{\text{e}} = \frac{d\hat{p}}{K_{\text{m}}^*} = \frac{d(p + s)}{(1 - D)K_{\text{m}}} \qquad (7)$$

where $\hat{p}$ is the mean effective stress for the microstructure; p is the net stress; and s is the suction.

The microstructural bulk modulus, K_{m}, is defined as

$$K_{\text{m}} = \frac{1 + e_{\text{m}}}{\kappa_{\text{m}}}(p + s) \qquad (8)$$

where e_{m} is the microstructural void ratio and κ_{m} is a model parameter.

The macrostructural deformations are affected by the microstructural deformations in an irreversible way (Gens & Alonso, 1992). A hypothesis of the model is that the plastic deformations of the macrostructure induced by microstructural effects are proportional to the microstructural strain according to the interaction functions, f_α. Two interaction functions f_α are defined in the case of suction decrease (MS) and suction increase (MC) (Fig. 12(b)), respectively. In this study, the following form is used

$$f_\alpha = f_{\alpha 0} + f_{\alpha i}\left(1 - \frac{p}{p_0}\right)^{n_\alpha}; \quad \alpha = \text{s(swelling)}, \text{ c(contraction)} \qquad (9)$$

where $f_{\alpha 0}$, $f_{\alpha i}$, n_α are fitting parameters.

The interaction functions depend on the ratio p/p_0, with p_0 as the yield mean net stress at the current macrostructural suction value.

The total plastic macrostructural strain ($\varepsilon_{\text{vM}}^{\text{p}}$) is obtained as the sum of the inelastic deformations of the microstructure

Table 1. Hydraulic parameters

Constitutive law	Parameter	Units	Value
Retention curve $$S_{\text{e}} = \frac{S_{\text{l}} - S_{\text{lr}}}{S_{\text{ls}} - S_{\text{lr}}} = \left[1 + \left(\frac{P_{\text{g}} - P_{\text{l}}}{P_0}\right)^{1/(1-\lambda)}\right]^{-\lambda}$$	P_0 λ S_{ls} S_{rl}	MPa — — —	4·026 0·26 1 0·01
Intrinsic permeability $$k_{\text{M}} = k_0 \frac{\phi_{\text{M}}^3}{(1 - \phi_{\text{M}})^2}\frac{(1 - \phi_0)^2}{\phi_0^3}$$	k_0 ϕ_0 ϕ_{min}	m^2 — —	$4{\cdot}94 \times 10^{-21}$ 0·269 0·01
Relative permeability $k_{\text{rj}} = S_{\text{ej}}^\lambda$	λ S_{ls} S_{lr}	— — —	3 1 0·01

through the interaction mechanism, and the plastic deformations (ε_{vLC}^p) induced when yielding of the macrostructure takes place (when the stress path reaches the loading collapse (LC) curve defined in the BBM model)

$$d\varepsilon_{vM}^p = d\varepsilon_{vLC}^p + f_\alpha \, d\varepsilon_{vm}^e \qquad (10)$$
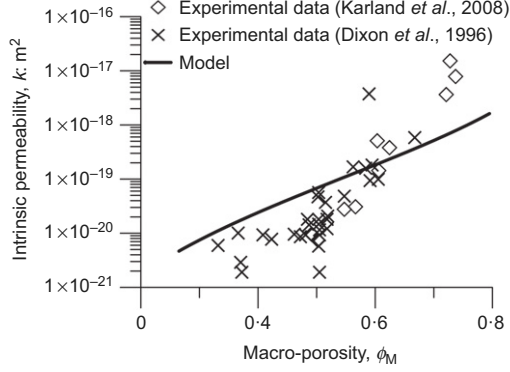

Fig. 14. Intrinsic permeability variation of MX80 pure bentonite with macro-porosity: experimental results (Dixon *et al.*, 1996; Karnland *et al.*, 2008) and model fitting

Hydraulic constitutive equations

The formulation assumes that the microstructural level is saturated even at relatively high suctions, which can be supported by the high affinity of the active clay minerals to water. The macro-pores are considered to be partially filled with the liquid phase. In this work, hydraulic equilibrium between the two continua is assumed.

Advective fluxes, governed by Darcy's law, are expressed as a function of the macrostructural permeability

$$q = -\frac{k_M k_{rM}}{\mu_M}(\nabla p + \rho_{wM}\boldsymbol{g}\nabla z) \qquad (11)$$

where q is the mass liquid flow (with respect to the solid phase); k_M is the macrostructural intrinsic permeability; k_{rM} is the relative permeability that expresses the effect of degree of saturation on global permeability; μ_M is the liquid viscosity; ρ_{wM} is water density; and $\boldsymbol{g}$ is the acceleration of gravity.

The dependency of intrinsic permeability on macro-porosity is assumed as

$$k_M = k_0 \frac{\phi_M^3}{(1-\phi_M)^2}\frac{(1-\phi_0)^2}{\phi_0^3} \qquad (12)$$
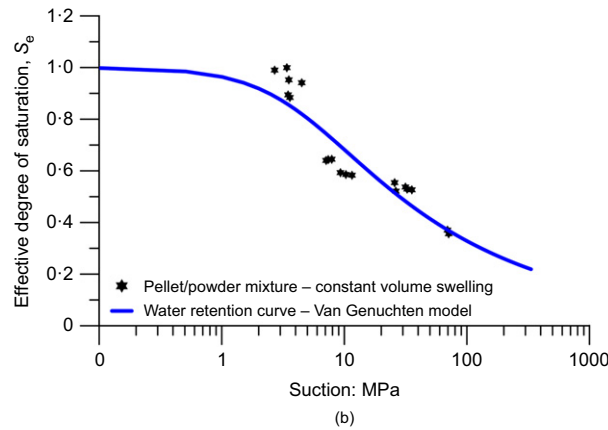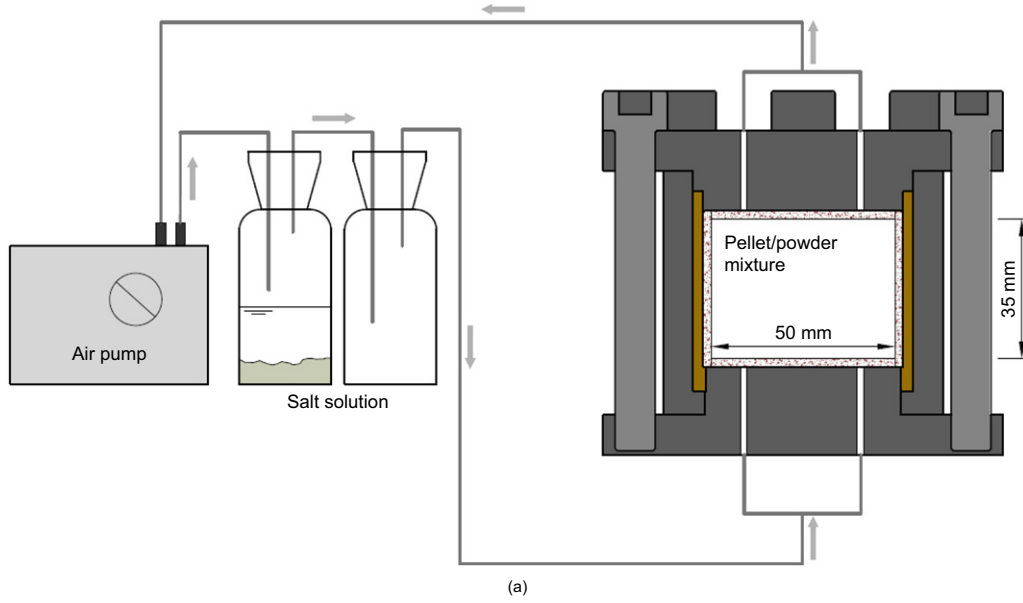

(a)

(b)

Fig. 15. (a) Schematic view of the special cell designed for determining the water retention curve under constant-volume conditions. (b) Water retention curve of a MX80 bentonite pellet/powder mixture prepared at dry density of 1·49 Mg/m³ under constant-volume conditions – experimental data and model fitting

8

where ϕ_M is the macro-porosity and k_0 is the reference intrinsic permeability at a reference porosity ϕ_0.

The dependency of relative permeability on degree of saturation is expressed as

$$k_{rM} = S_e^n \tag{13}$$

where n is a material parameter and S_e^n is the effective degree of saturation defined as

$$S_e = \frac{S_r - S_{lr}}{S_{ls} - S_{lr}} \tag{14}$$

where S_r is the degree of saturation; S_{lr} is the residual degree of saturation; and S_{ls} is the degree of saturation in saturated conditions.

The water retention model adopted for the macro-structure is

$$S_e = \frac{S_r - S_{rl}}{S_{sl} - S_{rl}} = \left[1 + \left(\frac{s}{P_0} \right)^{1/(1-\lambda)} \right]^{-\lambda} \tag{15}$$

where s is suction and P_0, λ are model parameters.

MODELLING THE 1/10 MOCK-UP TEST

The numerical analysis has been performed with a modified version of Code_Bright (Olivella *et al.*, 1996), which incorporates the double-structure elasto-plastic model for heterogeneous expansive clays and damage equations.

Determination of hydro-mechanical parameters

The hydro-mechanical parameters of the model were determined from a series of laboratory tests performed on the MX80 bentonite pellet/powder mixture (80 pellets/20 powder in dry mass) (Molinero-Guerra *et al.*, 2016a, 2016b, 2017, 2018a, 2018b, 2018c; Chen *et al.*, 2018).

The hydraulic parameters are summarised in Table 1. Variations of intrinsic permeability with porosity (equation (12)) have been derived from permeability tests performed on compacted MX80 bentonite, compacted at different dry densities (Dixon *et al.*, 1996; Karnland *et al.*, 2008). Fig. 14 shows the experimental measurements together with the model fitting (equation (12)). The reference intrinsic permeability adopted is $k_0 = 4.94 \times 10^{-21}$ m^2 for a reference macro-porosity, $\phi_M = 0.269$.

The water retention curve under constant-volume conditions was obtained for the pellet/powder mixture prepared at a dry density of 1.49 Mg/m^3, using a special set-up which allows the suctions to be imposed on specimens of 50 mm dia. and 35 mm high by vapour transfer (Fig. 15(a)). The stainless steel cell designed allows vapour exchanges through the two metallic porous discs on both the top and bottom of the sample, and also through a cylindrical porous disc on the lateral surface of the sample. This design is expected to significantly accelerate the hydration of the sample by a vapour equilibrium technique. The mass of the sample was regularly measured. In a standard fashion, equilibrium was considered to have been achieved once the mass had stabilised. Once equilibrium was reached both the water content and the suction were measured by oven drying with a chilled mirror dew-point tensiometer (Decagon, WP4).

The experimental results are displayed in Fig. 15(b), together with the model fitting (equation (15)).

The parameters for the mechanical behaviour are summarised in Table 2. Molinero-Guerra *et al.* (2017) measured volume changes of pellets equilibrated at

Table 2. Mechanical parameters

Constitutive law	Parameter	
Macrostructure Elastic part $d\varepsilon_{vM}^e = \left(\dfrac{\kappa}{1+e_M} \right) \dfrac{dp}{p} + \left(\dfrac{\kappa_s}{1+e_M} \right) \dfrac{ds}{s+p_{atm}}$	κ κ_s	0·028 0·001
Yield locus $p_0 = p_c \left(\dfrac{p_0^*}{p_c} \right)^{[\lambda(0)-\kappa]/[\lambda(s)-\kappa]}$ $\lambda(s) = \lambda(0) \left[r + (1-r)e^{-\beta s} \right]$	p_0^* : MPa p_c : MPa r $\lambda(0)$ β : MPa^{-1}	1·737 0·6 0·75 0·222 0·1
Microstructure Microstructural behaviour $K_m^* = \dfrac{1+e_m}{\kappa_m} \hat{p}$	κ_m	0·04
Damage model $K_m^* = (1-D)K_m; \ D(s) = \dfrac{\beta_d \ln(\alpha_d s^2 + 1)}{(s+p_{atm})^{\beta_d/\alpha_d}}$	α_d β_d	0·58 0·6
Interaction function (micro-swelling) $f_s = f_{s0} + f_{s1} \left(1 - \dfrac{p}{p_0} \right)^{n_s}$	f_{s0} f_{s1} n_s	−0·3 2·19 2·4
Interaction function (macro-swelling) $f_c = f_{c0} + f_{c1} \left(\dfrac{p}{p_0} \right)^{n_c}$	f_{c0} f_{c1} n_c	−0·29 2·19 0·5

different suctions by hydrostatic weighting waxed specimens into water. Total volumetric deformations of the samples were calculated from their volume. The microstructural
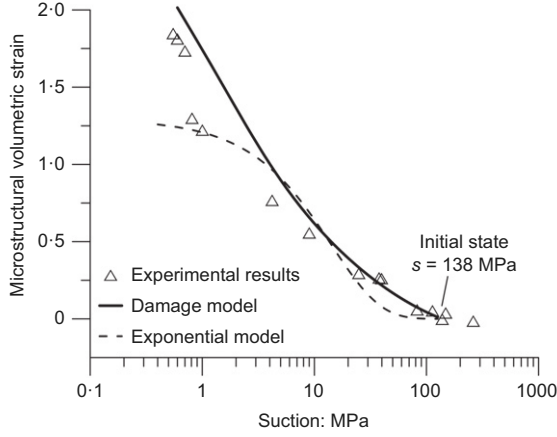

Fig. 16. Microstructural volumetric strain evolution upon wetting under free swelling conditions of MX80 bentonite pellets. Experimental data and the proposed damage model

volume deformation was determined by subtracting the cracking-induced deformation (using MIP data) from the total volumetric deformation. The measured and calculated (equation (7)) microstructural volumetric strains at different suction values are compared in Fig. 16 together with a model fitting at $D = 0$. Clearly, the non-consideration of damage ($D = 0$) fails in predicting the pellets' swelling deformation.

The microstructural parameter defining the microstructural bulk modulus used to calibrate the experimental data was estimated to $\kappa_m = 0.06$ (Fig. 16). The parameters for the damage description (equation (6)) were estimated at $\alpha_d = 0.58$, $\beta_d = 0.6$ (Fig. 13).

The compressibility parameters for the macrostructure and the variation of yield stress with suction were determined using the results from suction-controlled oedometer tests performed on the mixture of pellets and powder placed in a cell 35 mm high and 50 mm dia. (Molinero-Guerra et al., 2017; Chen et al., 2018). Three tests were carried out under three different suctions (0 MPa, 9 MPa and 138 MPa). While zero suction was imposed by circulating pure water, high suction values were imposed by circulating vapour at controlled relative humidity through the base of the sample (Fig. 17(a)). A high-pressure oedometer was used, allowing application of vertical stresses as high as 50 MPa.
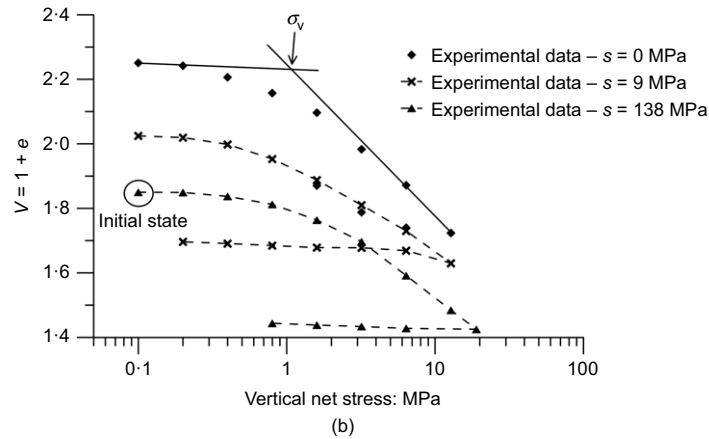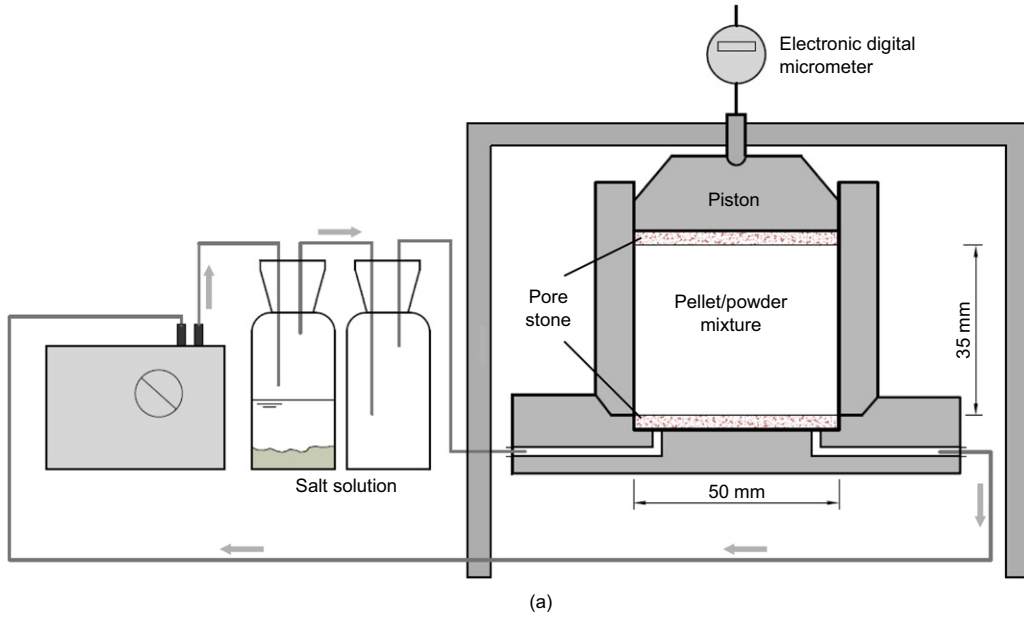

(a)

(b)

Fig. 17. (a) Experimental set-up for suction-controlled oedometer tests. (b) Results from suction-controlled oedometer tests on MX80 pellet/powder bentonite mixture (80/20) prepared at a dry density equal to 1·49 Mg/m^3
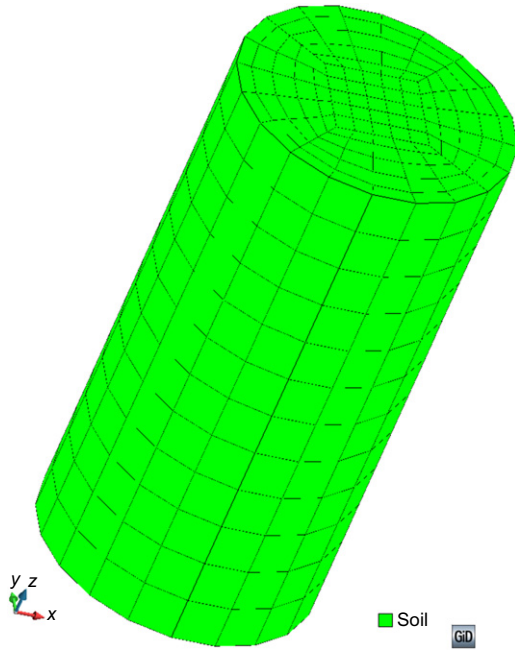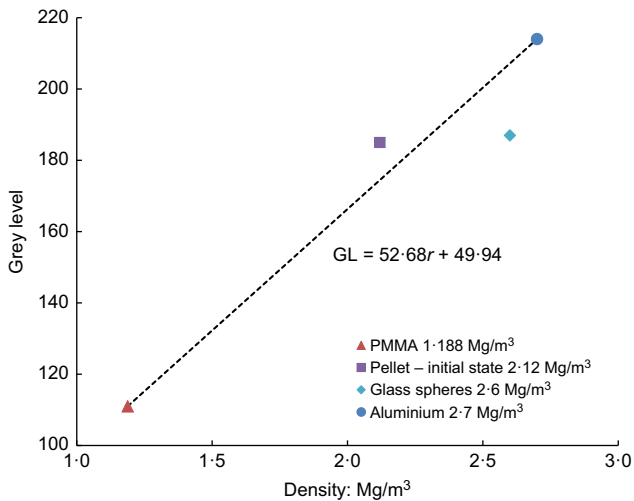
Fig. 18. Model geometry and mesh

Fig. 19. Correlation plot between density and grey level obtained from the μ-CT observations

Each test consisted of a wetting path followed by a loading/unloading path. Prior to compression, time was allowed until swelling stabilised (equilibrium was considered when the vertical displacement was lower than 0·01 mm during 8 h) under the imposed value of suction and a low vertical stress of 0·1 MPa. The results obtained were used to derive the compressibility parameters (κ, $\lambda(0)$ and $\lambda(s)$) (Table 2).

Geometry and boundary conditions

The 1/10 mock-up test is simulated using the proposed model outlined above and the hydro-mechanical parameters are summarised in Tables 1 and 2. The hydro-mechanical coupled analysis had been performed on a 3D finite-element geometry (Fig. 18). A mechanical boundary condition restraining displacement is assigned at the outer surfaces of the model domain. A water pressure of 0 MPa is imposed at the top and the bottom of the geometry to simulate hydration of the sample.

Estimation of the initial heterogeneous porosity field

Since no μ-CT observations were performed on the sample tested within the stainless steel mock-up cell, estimations of initial heterogeneous porosity fields were undertaken by image analysis of μ-CT scans carried out on three MX80 bentonite pellet/powder mixtures prepared at $\rho_d = 1·49$ Mg/m^3 and $s = 138$ MPa and tested within a PMMA mock-up cell (Fig. 9(a)). The technique of μ-CT uses X-ray projections of the same sample at many different angles allowing the reconstruction of a 3D view of the sample. The visualised parameter is the linear X-ray attenuation coefficient represented as a grey level. This parameter depends on the density, the atomic number and the X-ray energy used. The latter parameter is kept constant when scanning the bentonite at several time intervals. To derive correlation between mean grey levels and density (Fig. 19), reference elements with a known density consisting of two glass spheres and an element of aluminium were introduced into the mixture of MX80 bentonite and pellets (Van Geet *et al.*, 2005). To quantify porosity distribution, the mean grey value corresponding to each finite element was calculated then converted into apparent density using the calibration presented in Fig. 19. Total porosity corresponding to each finite-element volume is calculated and used to deduce macro-porosity at each finite element assuming that micro-porosity is homogeneously distributed.

Figure 20 displays initial heterogeneous porosity fields of the three scanned samples. For the three cases, the experimental variograms are shown in Fig. 21. The covariance function was calculated along the sample axis to obtain an insight into the impact of the preparation protocol (the samples were prepared by placing the mixture layer by layer into the cell) on porosity distribution.

A non-stationary variogram is obtained for sample 3. For samples 1 and 2 no spatial correlation is observed beyond 30 mm (sample 1) and 22 mm (sample 2), indicating a random distribution of porosity within the remaining domain of samples, which confirms that preparing samples at the same mean dry density with the same preparation protocol does not ensure similar spatial distribution of porosity within the mixture.

Modelling results

The estimated porosity fields were used to simulate the 1/10 mock-up test. The measured and predicted axial and radial swelling pressure evolutions for the three cases are displayed in Fig. 22. For completeness, the homogeneous case with no spatial variation of porosity (constant porosity equal 0·462) is compared to the results. Interestingly, the model predictions in case 1 (sample 1) appears to satisfactorily match the experimental results, except for sensor SP100. This indicates that the porosity field in this case corresponds to the best estimate of the structural distribution of the sample. In general, the rate and the magnitude of the swelling pressure are overestimated in cases 2 and 3, and in the homogeneous case. In spite of the highly heterogeneous structural distribution, the pattern of behaviour is very similar in all positions (except at SP100). The swelling pressure increases at different rates depending on the distance to the hydration front, then reaches a nearly stationary value after 200 days. At SP100 located at 20 mm from the top hydration front, the measurements show that the swelling pressure increased very rapidly and reached a peak of about
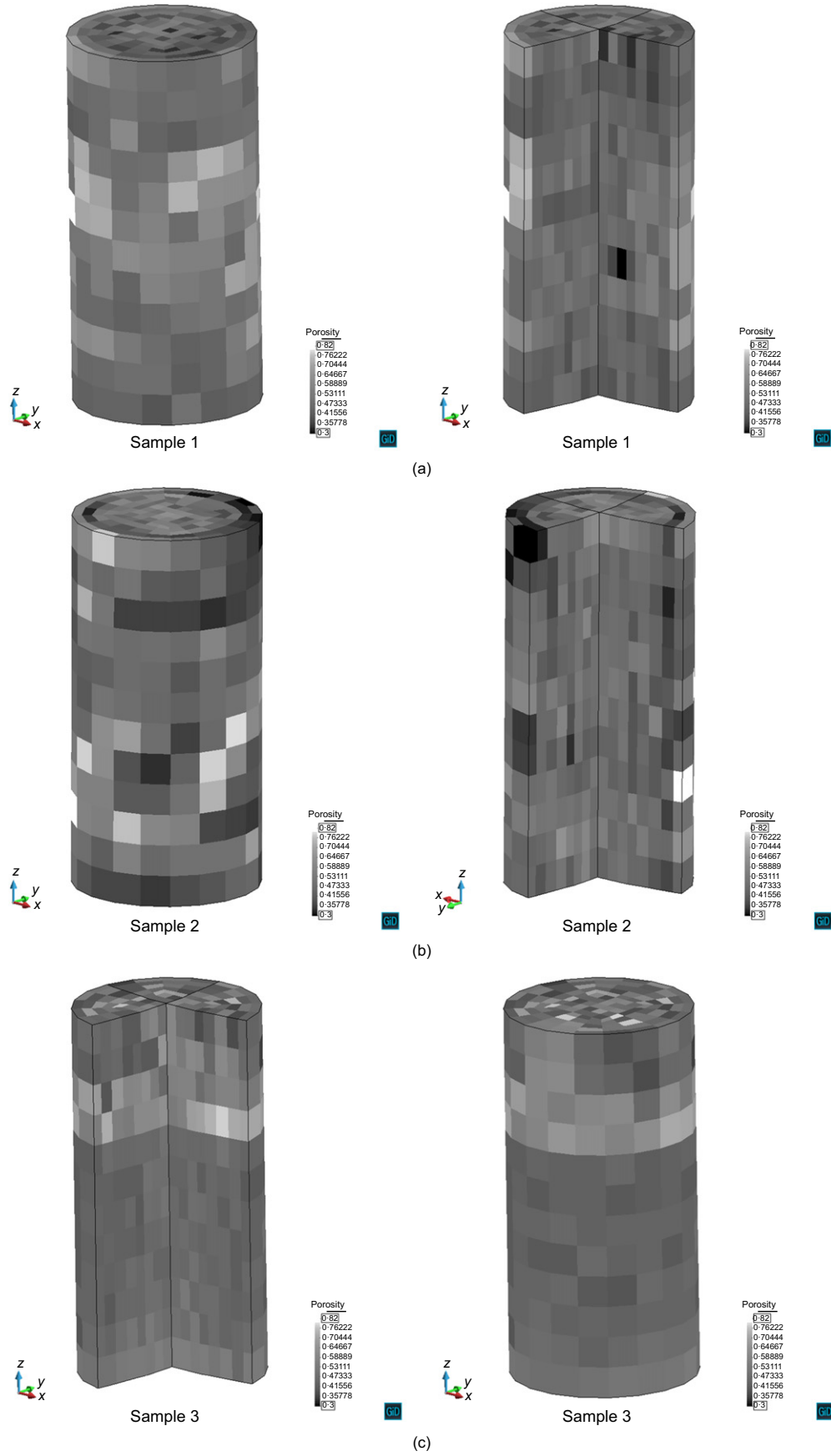
Fig 20. Initial total porosity of the three samples: (a) sample 1; (b) sample 2; (c) sample 3

2·1 MPa (Fig. 23). After about 5 h a significant decrease of the swelling pressure occurred towards a minimum value of 1·5 MPa (Fig. 23). The swelling pressure increased again at a slower rate and reached a value of 2·55 MPa after 60 days. Afterwards, the swelling pressure increased and stabilised at 3·3 MPa after 200 days (Fig. 22). The peak occurrence
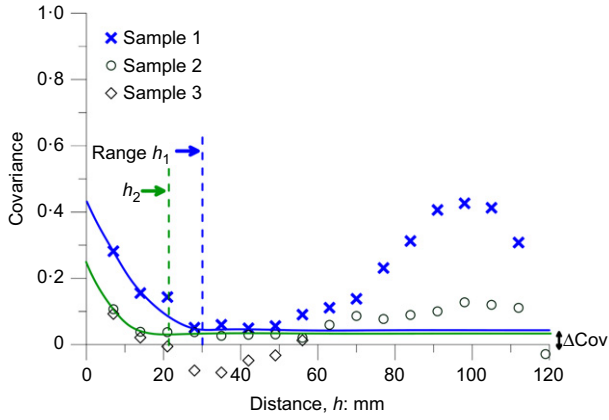
Fig. 21. Covariance of the total porosity following the vertical direction of the three investigated samples – variogram

followed by a decrease of the swelling pressure corresponds to the reorganisation of the microstructure characterised by the collapse of the macrospores between the bentonite grains. For this case, the model estimates well the magnitude of the swelling pressure, but fails in predicting the initial peak occurrence. This suggests that, at this zone, differences might exist between the real and the estimated porosity distributions.

The final values of radial swelling pressure are in the range of 3·3–4·4 MPa. It is worth noting that the radial swelling pressure measurements are strongly influenced by the local microstructural distribution at the vicinity of the sensors. The non-peak occurrences at SP40, SP60 and SP80 suggest that the sensors were placed in zones where high-density pellets are tightly arranged with a few or no grains of bentonite powder in between (Fig. 24). Similar trends were observed for the axial swelling pressure but with
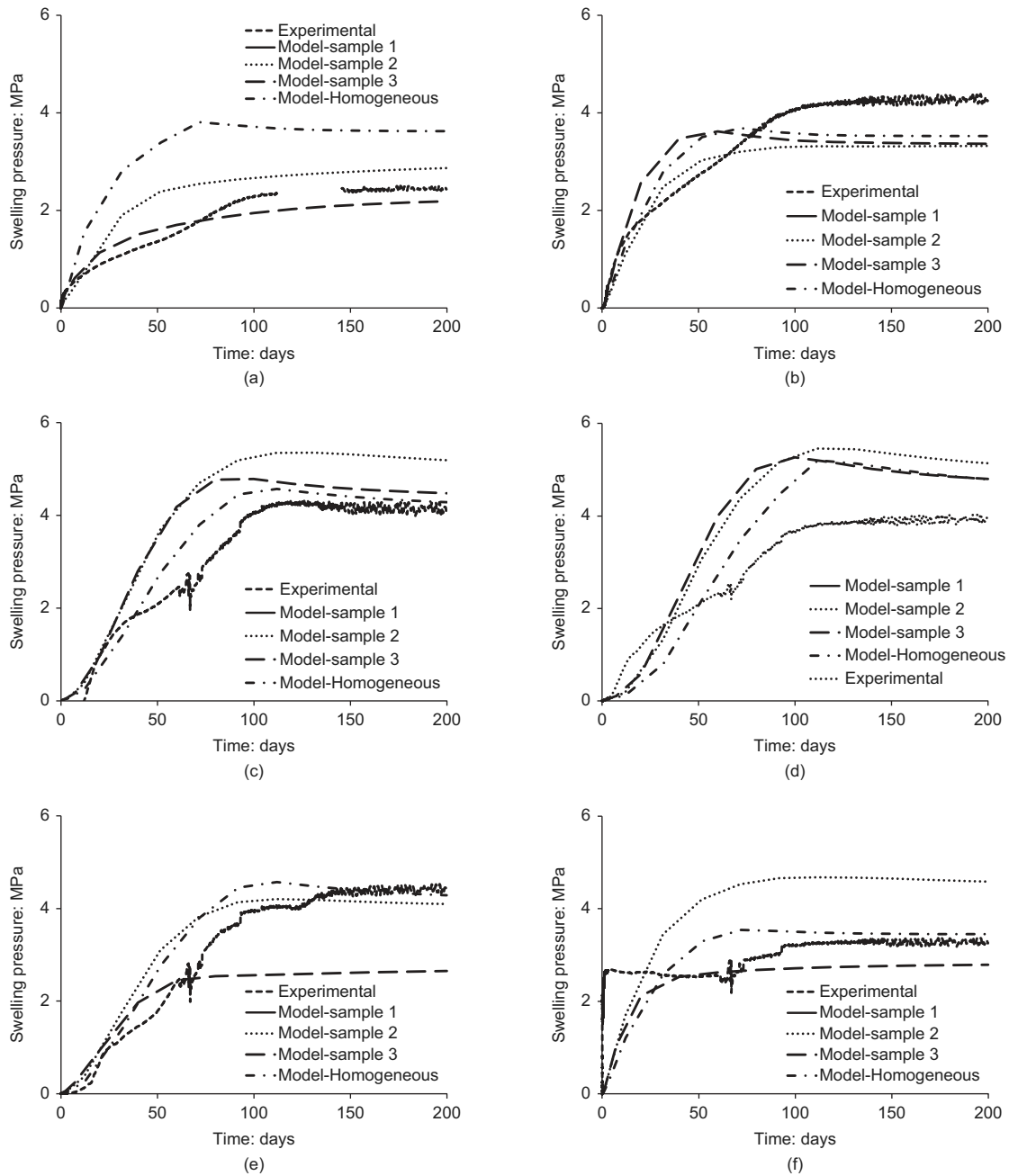

Fig. 22. Evolution of swelling pressure at different positions for the mock-up test together with model results of three different samples and a homogenous case: (a) axial; (b) SP20; (c) SP40; (d) SP60; (e) SP80; (f) SP100
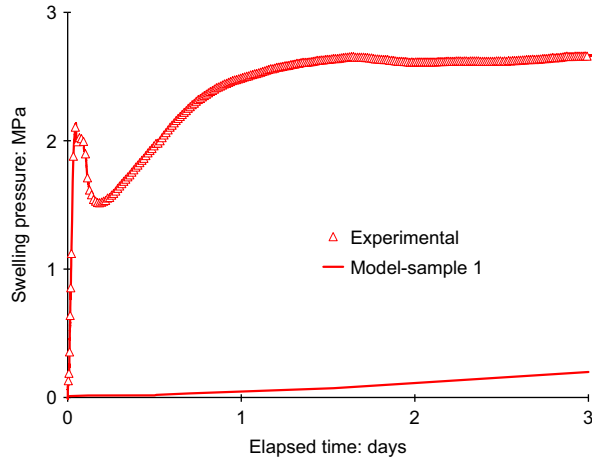
13

Fig. 23. Evolution of radial swelling pressure at SP100 during the first 4 days – experimental and modelling results
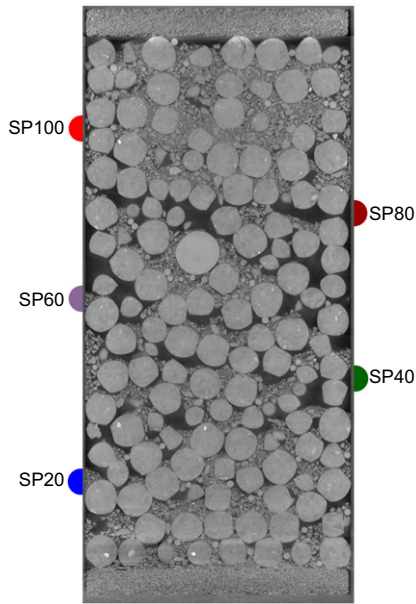

Fig. 24. Vertical section of sample 1 with the position of the radial swelling pressure sensors

a lower final value of about 2·45 MPa. No macrostructural collapse is observed in this case, indicating that collapse in some zones is compensated by the non-collapsing behaviour of other zones.

The radial and axial swelling pressures are not identical. The final values of radial swelling pressure are in the range of 3·3–4·4 MPa, while a lower final value of about 2·45 MPa is reached for the axial swelling pressure. A high anisotropic coefficient, C_a ($C_a = p_h/p_v$), ranging from 1·25 to 1·65 is obtained. This anisotropy is a consequence of the highly heterogeneous microstructural distribution of the mixture.

As the modelling of case 1 appears to be the most satisfactory, interesting information might be obtained by analysing in more detail some of the modelling results.

Figure 25 displays the calculated macro- and micro-porosities at initial state and after 200 days along three radial lines at 20 mm (R20), 60 mm (R60) and 100 mm (R100) from the bottom hydration face. Initially, different distributions of macro-porosity are observed along the three profiles with a concentration of large macro-pores at the sample boundary. Upon hydration there is a reduction of macro-pores while the microstructure is expanding. It has to be noted that the evolution of the macro-porosity results from two competing phenomena. Cracking of the pellets during swelling induces an increase of macro-pores. Simultaneously, the macro-pores are progressively invaded by the swollen bentonite particles. After 200 days, the macro-porosity is reduced progressively, with a concentration of large macro-pores within the central zone at R20 and R100. On the contrary, at R60 although the difference between the central part and the boundary reduces, large macro-pores are still located at the sample boundary.

In order to explore the long-term homogenisation of the mixture, the radial profiles (R20, R60 and R100) and distributions of dry density at different times (0, 200 and 5000 days) and sections are displayed in Figs 26 and 27, respectively. A heterogeneous distribution of dry density is observed. For a given hydration time, at R20, R60 and R100 low densities prevail at the outer boundaries due to the concentration at this zone of large macro-pores (Fig. 25). Dry density increases progressively deeper within the sample with a minimum value toward the central zone. An inverse gradient is observed along R60 further from the hydration

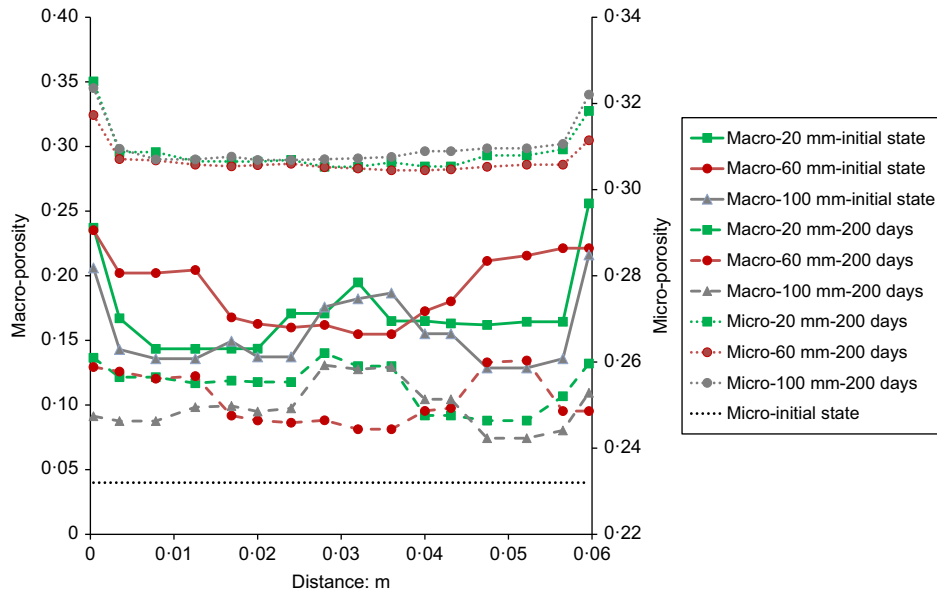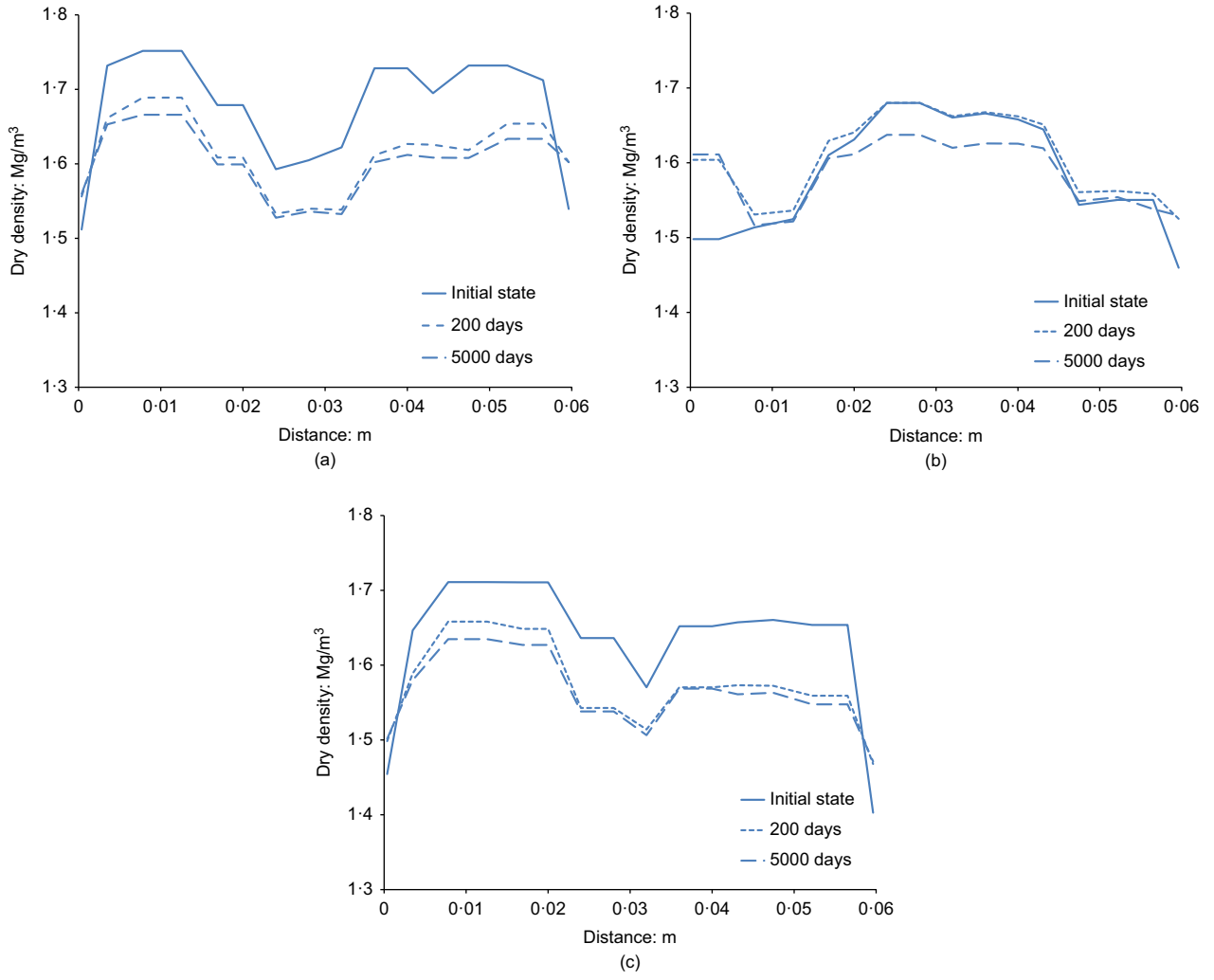**Fig. 25. Profiles of macro- and micro-porosities for sample 1 at different positions and times**

Fig. 26. Profiles of dry density for sample 1 at different positions after 200 days and 5000 days of hydration: (a) section at $z = 100$ mm; (b) section at $z = 60$ mm; (c) section at $z = 20$ mm
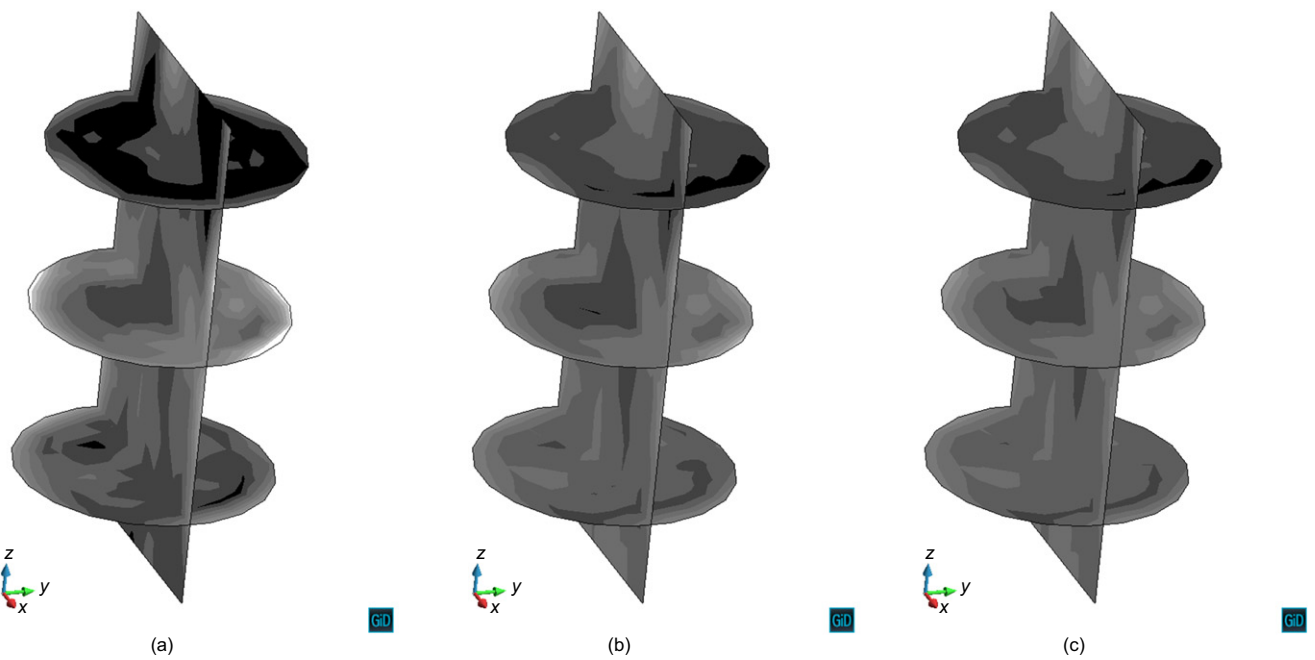

Fig. 27. Contours of dry density at different hydration times: (a) initial; (b) 200 days; (c) 5000 days
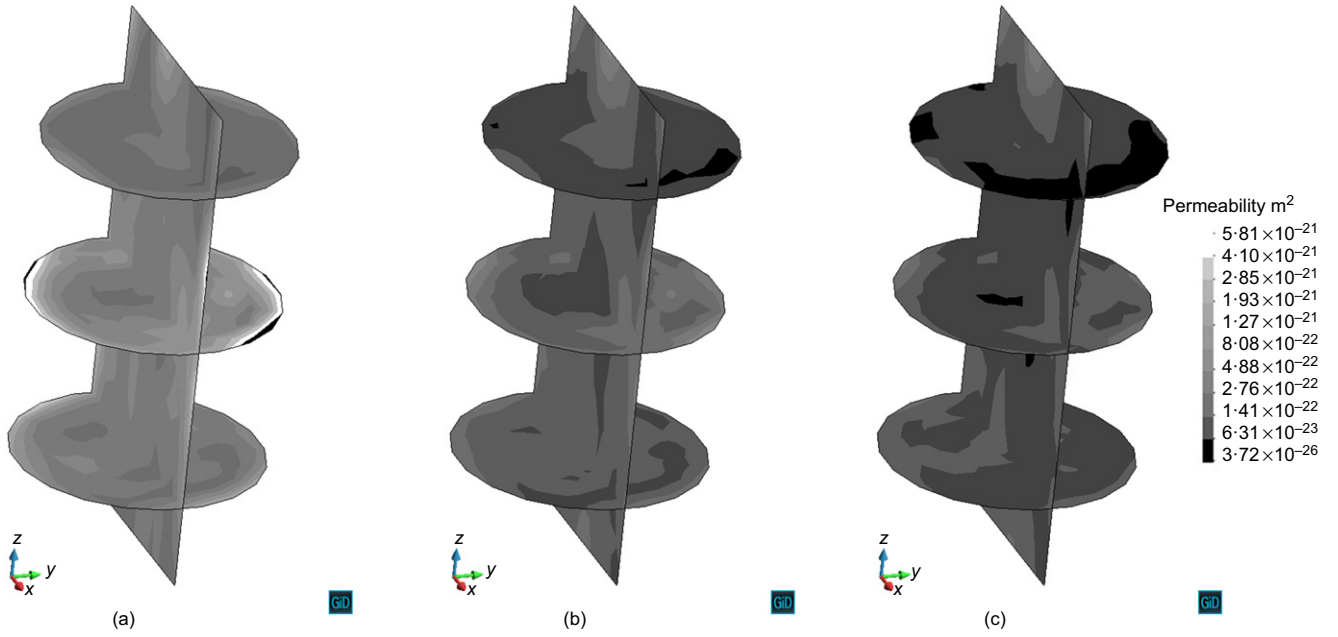
Fig. 28. Contours of permeability at different hydration times: (a) initial; (b) 200 days; (c) 5000 days
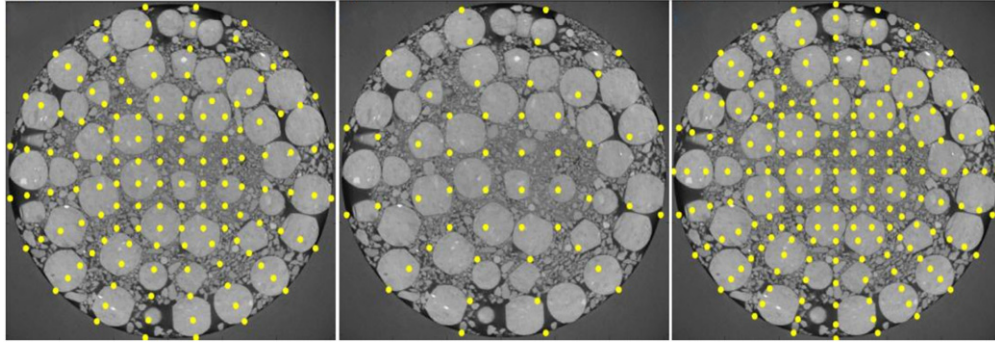

Fig. 29. Horizontal section of the sample 1 and finite-element nodes corresponding to three finite-element meshes used in the analysis

ends where dry density increases progressively toward the centre of the sample. As saturation progresses, the density gradients decrease but, at 5000 days, there are still remaining differences over the cross-sections of the sample (Fig. 27). After 5000 days of hydration, along R20, ρ_d values range from 1·47 Mg/m^3 to 1·63 Mg/m^3, while along R60, ρ_d values range from 1·51 Mg/m^3 to 1·62 Mg/m^3.

Interesting information on the hydration process can be obtained by analysing the impact of the heterogeneous structural distribution on intrinsic permeability (k). Fig. 28 shows the distributions of k at different times (0, 200 and 5000 days). At early hydration times, higher permeability is predicted at the outer boundaries of the sample due to the localisation of large macro-pores in this zone. This tendency is reversed when, under constant-volume conditions, the progressive clogging of macro-pores due to microstructural swelling leads to a potentially large reduction in intrinsic permeability, which significantly delays the mixture hydration. At the long term (after 5000 days), the permeability gradients within the sample are reduced, but still exist over the cross-sections of the sample (Fig. 28).

Mesh size effect

As the porosity field estimation is linked to the model finite-element mesh, three different mesh sizes have been considered to analyse their possible influence on modelling results. Two porosity distribution fields of sample 1 were determined by considering two different mesh sizes (coarser and more refined mesh than for case 1). Fig. 29 shows a horizontal section of sample 1 and the finite-element nodes corresponding to the two finite-element meshes.

Figure 30 depicts the evolution of swelling pressure for the two additional cases together with case 1. No significant differences are observed, indicating that the size mesh effect is negligible.

CONCLUDING REMARKS

The hydro-mechanical behaviour of MX80 bentonite pellet/powder mixture (80/20 in dry mass) intended as a sealing material in underground repositories for radioactive waste was analysed by using a double-structure formulation which considers the initial heterogeneous structural distribution of the mixture and the wetting-induced damage to the pellets. The model parameters were determined based on laboratory experimental results. The proposed model was then used to simulate a 1/10 scale mock-up test. In order to ensure a good representation of the initial test conditions, the initial heterogeneous distribution of the bentonite pellets/powder mixture was appropriately estimated from
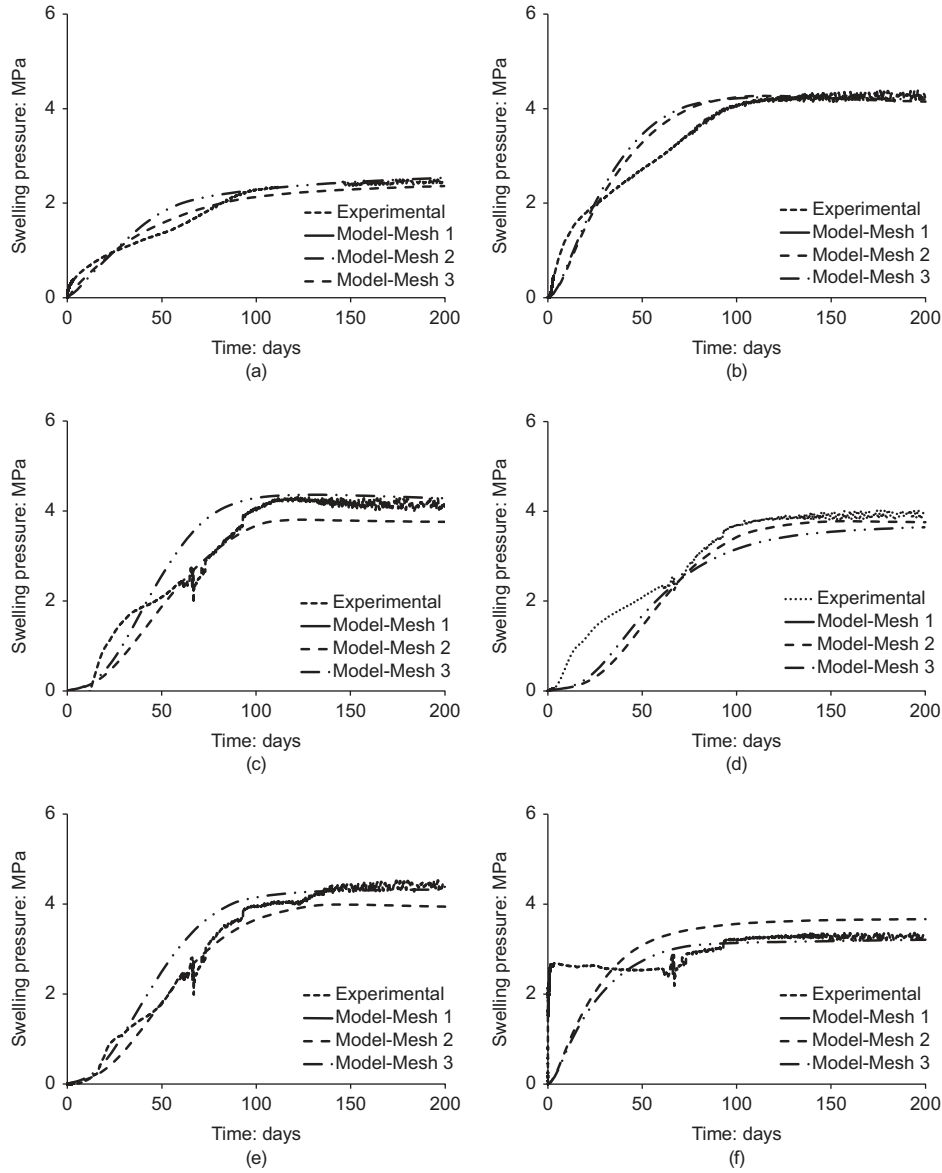
Fig. 30. Evolution of the swelling pressure at different positions with time – experimental data and model results with different mesh sizes: (a) axial; (b) SP20; (c) SP40; (d) SP60; (e) SP80; (f) SP100

μ-CT observations. The analysis carried out has demonstrated a number of interesting features.

The evolution rates of axial swelling pressure were significantly lower than the radial ones. This difference is attributed to the initial heterogeneous structural distribution associated with the fabrication of the bentonite mixture sample. Model results demonstrated the long-term heterogeneous distribution of dry density. As hydration progresses, even though a decrease in dry density gradients is observed, there are still remaining differences in dry density over the cross-section of the bentonite mixture after almost 13 years of hydration. The swelling anisotropy is maintained at the long term (decade). Additionally, the remaining dry density gradients induce significant (several orders of magnitude) differences in hydraulic conductivity, which should be considered in the evaluation of long-term performance.

NOTATION
D	damage coefficient
e	void ratio
e_m	microstructural void ratio
e_M^{mean}	mean macro void ratio
f_α	interaction functions
$f_{\alpha 0}$	fitting parameters
$f_{\alpha i}$	fitting parameters
$\boldsymbol{g}$	gravitational acceleration
K_m	microstructural bulk modulus
k_0	reference intrinsic permeability
k_M	elastic parameter for the macrostructure
k_M	macrostructural intrinsic permeability
k_{rM}	relative permeability
n	material parameter
n_α	fitting parameters
P_0	fitting parameter
p	net stress
$\hat{p}$	mean effective stress defined
p_0	yield mean net stress
p_{atm}	atmospheric pressure
p_0^*	saturated preconsolidation pressure
r	fitting parameters
s	suction
S_e^n	effective degree of saturation
S_{lr}	residual degree of saturation
S_{ls}	degree of saturation at saturated conditions
S_r	degree of saturation
α_d	fitting parameter

17

β fitting parameter
β_{d} fitting parameter
$\varepsilon_{\mathrm{v}}^{\mathrm{M}}$ macroscopic volumetric deformation
$\varepsilon_{\mathrm{vM}}^{\mathrm{p}}$ plastic macrostructural strain.
κ_{m} model parameter
λ fitting parameter
$\lambda(s)$ slope of virgin consolidation line
$\lambda(0)$ slope of virgin saturated consolidation line
μ_{M} liquid viscosity
ρ_{d} dry density
ρ_{wM} water density
ϕ_{cracks} porosity of cracks
ϕ_{M} macro-porosity
ϕ_{m} micro-porosity
ϕ_0 reference porosity

REFERENCES

Alonso, E. E., Gens, A. & Josa, A. (1990). A constitutive model for partially saturated soils. *Géotechnique* **40**, No. 3, 405–430, https://doi.org/10.1680/geot.1990.40.3.405.

Alonso, E. E., Gens, A. & Josa, A. (1999). Modelling the mechanical behaviour of expansive clays. *Engng Geol.* **54**, No. 1–2, 173–183.

Alonso, E. E., Olivella, S. & Arnedo, D. (2006). Mechanisms of gas transport in clay barriers. *J. Iberian Geol.* **32**, No. 2, 175–196.

Alonso, E. E., Romero, E. & Hoffmann, C. (2011). Hydromechanical behaviour of compacted granular expansive mixtures: experimental and constitutive study. *Géotechnique* **61**, No. 4, 329–344, https://doi.org/10.1680/geot.2011.61.4.329.

Barnichon, J. D. & Deleruyelle, F. (2009). Sealing experiments at the Tournemire URL. *Proceedings of Eurosafe forum 2009: safety implications of an increased demand for nuclear energy*, Brussels, Belgium.

Chen, Y., Cui, Y. J. & Molinero Guerra, A. (2018). Compression behavior of bentonite powder/pellet mixture. In *Proceedings of GeoShanghai 2018 international conference: multi-physics processes in soil mechanics and advances in geotechnical testing* (eds L. Hu, X. Gu, J. Tao and A. Zhou), pp. 39–46. Singapore: Springer.

Dixon, D. A., Gray, M. N. & Graham, J. (1996). Swelling and hydraulic properties of bentonites from Japan, Canada and USA. *Proceedings of the 2nd international congress on environmental geotechnics*, Osaka, Japan, pp. 5–8.

Gens, A. & Alonso, E. E. (1992). A framework for behavior of unsaturated expansive clays. *Can. Geotech. J.* **29**, No. 6, 1013–1032.

Gens, A., Vallejan, B., Sánchez, M., Imbert, C., Villar, M. V. & Van Geet, M. (2011). Hydromechanical behaviour of a heterogeneous compacted soil: experimental observations and modelling. *Géotechnique* **61**, No. 5, 367–386, https://doi.org/10.1680/geot.SIP11.P.015.

Imbert, C. & Villar, M. V. (2006). Hydro-mechanical response of a bentonite pellets/powder mixture upon infiltration. *Appl. Clay Sci.* **32**, No. 3–4, 197–209.

Karnland, O., Nilsson, U., Weber, H. & Wersin, P. (2008). Sealing ability of Wyoming bentonite pellets foreseen as buffer material-laboratory results. *Phys. Chem. Earth, Parts A/B/C* **33**, Suppl. 1, S472–S475.

Mokni, N. (2016). Analysis of hydro-mechanical behaviour of compacted bentonite/sand mixture using a double structure formulation. *Environ. Earth Sci.* **75**, No. 14, article 1087.

Mokni, N. & Barnichon, J. D. (2016). Hydro-mechanical analysis of SEALEX in situ tests-impact of technological gaps on long term performance of repository seals. *Engng Geol.* **205**, 81–92.

Molinero-Guerra, A., Mokni, N., Cui, Y. J., Tang, A. M., Aimedieu, P., Delage, P., Bernier, F. & Bornert, M. (2015). Water retention properties and microstructure of bentonite pellets/powder mixture. *Proceedings of international symposium on energy geotechnics*, Barcelona, Spain.

Molinero-Guerra, A., Mokni, N., Delage, P., Cui, Y. J., Tang, A. M., Aimedieu, P., Bernier, F. & Bornert, M. (2016a). In-depth characterisation of a mixture composed of powder/pellets MX80 bentonite. *Appl. Clay Sci.* **135**, 538–546.

Molinero-Guerra, A., Mokni, N., Delage, P., Cui, Y. J., Tang, A. M., Aimedieu, P., Bernier, F. & Bornert, M. (2016b). Experimental and digital characterizations of the hydro-mechanical behavior of a heterogeneous material, powder/pellets bentonite mixture. *Proceedings of PhD conference on radioactive waste management and geological disposal*, Delft, the Netherlands.

Molinero-Guerra, A., Mokni, N., Delage, P., Cui, Y. J., Tang, A. M., Aimedieu, P., Bernier, F. & Bornert, M. (2017). In-depth characterization of the hydro-mechanical behavior of a mixture composed of pellets/powder MX80 bentonite. *Proceedings of Pan-Am UNSAT 2017*, Dallas, TX, USA.

Molinero-Guerra, A., Cui, Y. J., Mokni, N., Delage, P., Bornert, M., Aimedieu, P., Tang, A. M. & Bernier, F. (2018a). Investigation of the hydro-mechanical behaviour of a pellet/powder MX80 bentonite mixture using an infiltration column. *Engng Geol.* **243**, 18–25.

Molinero-Guerra, A., Aimedieu, P., Bornert, M., Cui, Y. J., Tang, A. M., Sun, Z., Mokni, N., Delage, P. & Bernier, F. (2018b). Analysis of the structural changes of a pellet/powder bentonite mixture upon wetting by X-ray computed micro-tomography. *Appl. Clay Sci.* **165**, 164–169.

Molinero-Guerra, A., Mokni, N., Delage, P., Cui, Y. J., Tang, A. M., Aimedieu, P., Bernier, F. & Bornert, M. (2018c). Experimental characterizations of the hydro-mechanical behavior of a pellet/powder bentonite mixture. *Proceedings of UNSAT 2018*, Hong Kong, China.

Olivella, S., Gens, A., Carrera, J. & Alonso, E. E. (1996). Numerical formulation for a simulator (CODE_BRIGHT) for the coupled analysis of saline media. *Engng Comp.* **13**, No. 7, 87–112.

Pusch, R. (1979). Highly compacted sodium bentonite for isolating rock-deposited radio- active waste products. *Nucl. Technol.* **45**, No. 2, 153–157.

Saba, S., Cui, Y. J. & Barnichon, J. D. (2014a). Investigation of the swelling behaviour of compacted bentonite–sand mixture by mock-up tests. *Can. Geotech. J.* **51**, No. 12, 1399–1412.

Saba, S., Delage, P., Lenoir, N., Cui, Y. J., Tang, A. M. & Barnichon, J. D. (2014b). Further insight into the microstructure of compacted bentonite/sand mixture. *Engng Geol.* **168**, 141–148.

Sanchez, M., Gens, A., Guimaraes, L. & Olivella, S. (2005). A double structure generalized plasticity model for expansive materials. *Int. J. Numer. Analyt. Methods Geomech.* **29**, No. 8, 751–787.

Van Geet, M., Volckaert, G. & Roels, S. (2005). The use of microfocus X-ray computed tomography in characterising the hydration of a clay pellet/powder mixture. *Appl. Clay Sci.* **29**, No. 2, 73–87.

Villar, M. V. (2008). *Thermo-hydro-mechanical characterisation of a bentonite from Cabo de Gata. A study applied to the use of bentonite as sealing material in high level radioactive waste repositories*, Publicación Técnica ENRESA 01/2002. Madrid, Spain: ENRESA.

Wang, Q., Tang, A. M., Cui, Y. J., Barnichon, J. D. & Ye, W. M. (2013). Investigation of the hydro-mechanical behaviour of compacted bentonite/sand mixture based on the BExM model. *Comput. Geotech.* **54**, 46–52.

Wieczorek, K., Gaus, I., Mayor, J. C., Schuster, K., J. L. García-Siñeriz, J. C. & Sakaki, T. (2017). *In situ* experiments on bentonite-based buffer and sealing materials at the Mont Terri rock laboratory (Switzerland). *Swiss J. Geosci.* **110**, No. 1, 253–268.

Yong, R. N., Boonsinsuk, P. & Wong, G. (1986). Formulation of backfill material for a nuclear fuel waste disposal vault. *Can. Geotech. J.* **23**, No. 2, 216–228.